

OPEN

Equatorial Pacific seawater $p\text{CO}_2$ variability since the last glacial period

Kaoru Kubota¹, Yusuke Yokoyama², Tsuyoshi Ishikawa¹, Takuya Sagawa³, Minoru Ikehara⁴ & Toshitsugu Yamazaki²

The ocean may have played a central role in the atmospheric $p\text{CO}_2$ rise during the last deglaciation. However, evidence on where carbon was exchanged between the ocean and the atmosphere in this period is still lacking, hampering our understanding of global carbon cycle on glacial–interglacial timescales. Here we report a new surface seawater $p\text{CO}_2$ reconstruction for the western equatorial Pacific Ocean based on boron isotope analysis—a seawater $p\text{CO}_2$ proxy—using two species of near-surface dwelling foraminifera from the same marine sediment core. The results indicate that the region remained a modest CO_2 sink throughout the last deglaciation.

During the last deglaciation (ca. 19.0–10.5 ka), the atmospheric partial pressure of carbon dioxide ($p\text{CO}_2$) increased by approximately $80 \mu\text{atm}^{1-3}$. Lines of evidence suggest that the deep-ocean carbon reservoir played a central role in the rise in atmospheric CO_2 , since its carbon storage capacity is 60 times larger than that of the atmosphere⁴⁻⁸. However, evidence on where carbon was exchanged between the ocean and the atmosphere is still lacking, hampering our understanding of global carbon cycle on glacial–interglacial timescales.

The boron isotope ratio ($\delta^{11}\text{B}$) of the skeletons of marine calcifying organisms such as corals and foraminifera can be used to infer where a CO_2 source or sink existed, because the $\delta^{11}\text{B}$ value of marine calcium carbonates is dependent on seawater pH, from which the $p\text{CO}_2$ of the seawater can be reconstructed⁹⁻¹². Investigating current oceanic source regions of CO_2 , such as the equatorial Pacific, is of great importance because such regions were likely sites of CO_2 transfer from the deep-sea to the atmosphere in the past, as they are today (Fig. 1). In previous studies that measured $\delta^{11}\text{B}$ in biogenic calcium carbonates, Martinez-Boti *et al.*¹⁰ (ODP Site 1238, Fig. 1) and Kubota *et al.*¹¹ (IODP Exp. 310) revealed that central and eastern parts of the equatorial Pacific (CEP and EEP, respectively) acted as CO_2 sources during the last deglaciation, suggesting that the equatorial Pacific ocean partly contributed to the rise in atmospheric CO_2 . However, some controversial results have been obtained in a marine sediment record from the western equatorial Pacific (WEP)¹². Based on $\delta^{11}\text{B}$ measurements of the planktonic foraminifera *Torilobatus sacculifer* in a marine sediment core (ERDC-92, Fig. 1), Palmer and Pearson¹² reported that the surface layer of the WEP was a CO_2 source during the last deglaciation, which suggested a potential contribution of this region to the deglacial rise in atmospheric CO_2 . However, their reported ranges of $\delta^{11}\text{B}$ values differ from generally accepted values for *T. sacculifer* on glacial–interglacial timescales^{9,10,13-16} by as much as 5‰, which is likely due to positive bias, especially when analyzing foraminifera shell using negative thermal ionization mass spectrometry (N-TIMS)^{15,17-19}. Considering that glacial–interglacial changes in $\delta^{11}\text{B}$ measured in foraminifera are as small as approximately 2‰, this large discrepancy cannot be overlooked. The $\delta^{11}\text{B}$ measurement of biogenic calcium carbonate using N-TIMS method has started since the end of 1980s (ref.²⁰), and there has been a significant development in analytical procedure¹⁵⁻¹⁹. However, it still suffers from mass fractionation during ionization of the sample, resulting in a larger analytical uncertainty as well as less accuracy, especially when foraminifera sample is analyzed¹⁷⁻¹⁹. The $\delta^{11}\text{B}$ measurement using multi-collector inductively coupled plasma mass spectrometry (MC-ICPMS) has started since the beginning of 2000s (refs^{21,22}), which has become more widely-accepted and conventional ways to determine $\delta^{11}\text{B}$ values, providing more precise and accurate values (e.g., refs^{9-11,13-19,23,24}). Therefore, the refinement of seawater $p\text{CO}_2$ records derived from the $\delta^{11}\text{B}$ of planktonic foraminifera from the WEP, determined by MC-ICPMS method, is of great importance for understanding the role of the equatorial Pacific in the deglacial rise in atmospheric CO_2 . The WEP drives the world's most intense

¹Kochi Institute for Core Sample Research, Japan Agency for Marine–Earth Science and Technology, Nankoku, Japan.

²Atmosphere and Ocean Research Institute, The University of Tokyo, Kashiwa, Japan. ³Institute of Science and Engineering, Kanazawa University, Kanazawa, Japan. ⁴Center for Advanced Marine Core Research, Kochi University, Nankoku, Japan. Correspondence and requests for materials should be addressed to K.K. (email: kaoryu0129@gmail.com)

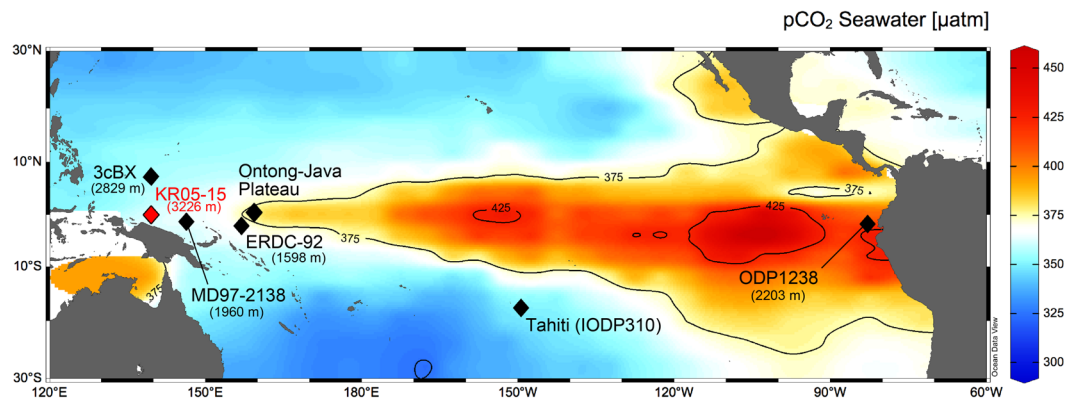


Figure 1. Sea surface $p\text{CO}_2$ in the equatorial Pacific. Equatorial Pacific locations discussed in the text with sea surface $p\text{CO}_2$ values for the reference year 2000 CE. Red and blue areas represent CO_2 sources and sinks, respectively⁴². Diamonds indicate the locations of marine sediment cores and fossil corals mentioned in this study.

atmospheric convection, being regarded as a heat engine of earth climate system²⁵, thus to understand past oceanographic variability is of great importance not only for carbon cycle but also for climatology. For this purpose, we chose a marine sediment core recovered from the West Caroline Basin (KR05-15 PC01, 0.10°S 139.58°E, 3226 m below sea level, Fig. 1)²⁶. A chronology of core KR05-15 PC01 was constructed based on 17 radiocarbon dates and deterministic age-depth modeling²⁷, as well as oxygen isotope measurements of benthic foraminifera shells (Supplementary Fig. 1).

Boron Isotopes and Seawater CO_2 System Reconstruction

In this study, we analyzed two species of surface-dwelling planktonic foraminifera—*Globigerinoides ruber* (white) and *T. sacculifer*. We collected foraminifera shells from size fractions generally used in paleoceanographic studies, namely, 300–355 μm and 500–855 μm , for *G. ruber* and *T. sacculifer* (with a sac-like final chamber), respectively^{9,10,13–16,24}. To calculate $p\text{CO}_2$, it is necessary to measure not only $\delta^{11}\text{B}$ but also the Mg/Ca ratio (a temperature proxy) and oxygen isotope ratio ($\delta^{18}\text{O}$, a salinity proxy). Thus, we established a way to obtain these three values from a single sample, which requires 3–7 mg of foraminifera shells, from which shells are removed that potentially contain fragments of shells from other calcifying organisms and siliciclastic grains (Supplementary Figs S2–S7).

The $\delta^{11}\text{B}$ values obtained in this study lie within the range obtained by Henehan *et al.*¹³ for both *G. ruber* and *T. sacculifer*, and are also consistent with the reported $\delta^{11}\text{B}$ values from the core-top material of marine sediment collected from the Ontong Java Plateau in the WEP¹⁴ (Fig. 1, Supplementary Fig. S7). Both foraminifera records show steady $\delta^{11}\text{B}$ values during the last glacial period (31–20 ka) (Fig. 2a), and both then show gradual decreases in $\delta^{11}\text{B}$, starting at the beginning of the last deglaciation, with the onset of the decrease in *T. sacculifer* preceding that in *G. ruber* by approximately 3 ky. Before 8 ka, the $\delta^{11}\text{B}$ values of *T. sacculifer* are always lower than those of *G. ruber*, with a difference of 1.0–1.5‰. We estimate the calcification depth of *G. ruber* and *T. sacculifer* from theoretically predicted $\delta^{18}\text{O}$ and $\delta^{11}\text{B}$ values using data spanning the Holocene (4.0–10.5 ka). Since water temperature and pH (and $p\text{CO}_2$) vary with water depth (Fig. 3a–c), the measured $\delta^{18}\text{O}$ and $\delta^{11}\text{B}$ values of foraminifera shells can be used to estimate the mean water depth at which the calcite shells precipitated. The theoretical $\delta^{18}\text{O}$ depth profile of foraminifera calcite is calculated from temperature and seawater $\delta^{18}\text{O}$ values. For the calculation of theoretical $\delta^{11}\text{B}$ depth profile of both species, seawater pH is used, in which a decrease of pH due to anthropogenic CO_2 incorporation since the Industrial Revolution is considered. The estimates of calcification depth based on different isotopes showed good agreement (Fig. 3d,e). Estimated calcification depths were 0–75 m (within the mixed layer) for *G. ruber*, and 75–125 m (below the mixed layer; upper thermocline) for *T. sacculifer* (Fig. 3), which is consistent with independent estimates from marine sediment cores collected in the WEP^{28–30}. In the present study, *T. sacculifer* shells recorded colder, lower pH, and higher $p\text{CO}_2$ water compared with *G. ruber* shells (Figs 2 and 3).

Shell Dissolution Effect

Because our core was obtained from water below the calcite saturation horizon depth (the saturation state with respect to calcite, Ω_{calcite} is 0.87), the bottom water is corrosive to calcite. We investigated the potential influence of dissolution of the *G. ruber* and *T. sacculifer* foraminifera shells on the $\delta^{18}\text{O}$ and $\delta^{11}\text{B}$ values, and thus on the mean calcification depth estimates and $p\text{CO}_2$ reconstructions.

For *G. ruber*, both $\delta^{18}\text{O}$ and $\delta^{11}\text{B}$ of the shell is insensitive to dissolution^{14,31–33} (Supplementary Text). This is also supported by the fact that the $\delta^{18}\text{O}$ variation of *G. ruber* in core KR05-15 PC01 carries an identical environmental signal to those collected from a nearby sediment core that has an excellent preservation of foraminifera shells (MD97-2138; Fig. 1, Supplementary Fig. S5)²⁹. For *T. sacculifer*, on the other hand, shell dissolution effects on its geochemistry is not as straightforward as *G. ruber*, which is because of a presence of the sac-like final chamber. The sac-like final chamber and a gametogenic calcite coating are precipitated during the last life stage of this animal^{30,33–37}. During the reproduction, they migrate into the thermocline depth and release gametes, which is governed by lunar cycles^{30,34,35,37}. The mean calcification depth of *T. sacculifer* in the WEP is deeper than

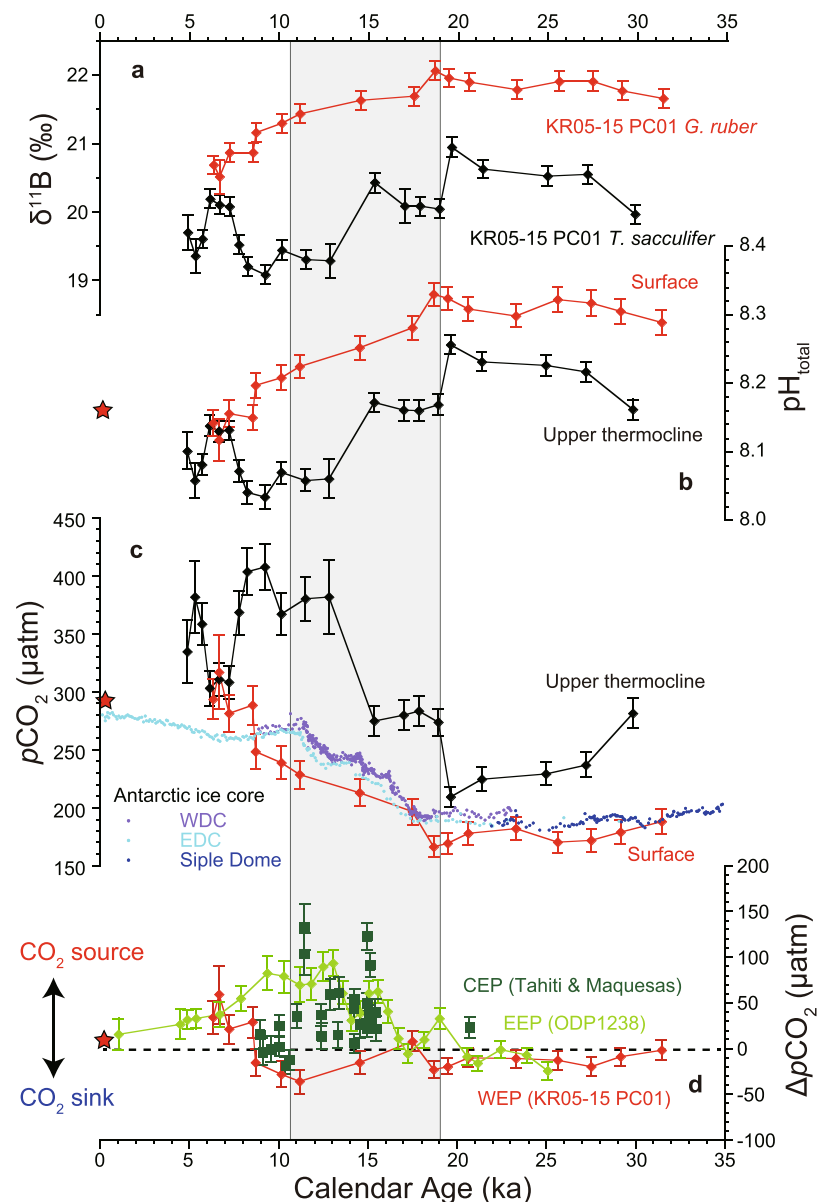


Figure 2. Deglacial changes of seawater CO₂ system. Deglacial $\delta^{11}\text{B}$, pH, pCO_2 , and ΔpCO_2 (seawater pCO_2 minus atmospheric pCO_2) variability in the equatorial Pacific. **(a)** $\delta^{11}\text{B}$ values of *G. ruber* (red) and *T. sacculifer* (black) from core KR05-15 PC01 with 2σ analytical uncertainty. **(b)** pH (in total hydrogen scale) of surface and upper-thermocline seawater reconstructed from $\delta^{11}\text{B}$. **(c)** Reconstructed pCO_2 of surface and upper-thermocline seawater and atmospheric pCO_2 reconstructed from Antarctic ice cores (West Antarctic Ice Sheet Divide ice core, WDC; Siple Dome; EPICA Dome C, EDC)^{1–3}. **(d)** Reconstructed pCO_2 of surface seawater in the WEP (red, this study), EEP (light green)¹⁰, and CEP (dark green)^{11,23}. Error bars of pH, pCO_2 , and ΔpCO_2 were calculated using a Monte Carlo approach. The shaded area indicates the time period of the last deglaciation.

global mean, likely due to thick mixed layer and chlorophyll maximum in the thermocline depth³⁰. For example, Rebotim *et al.*³⁷ estimate using plankton tow that the mean calcification depth of *T. sacculifer* is shallower in the subtropical North Atlantic, ~60 m. Furthermore, the sac is likely more resistant to corrosive bottom water, thus the measurement of *T. sacculifer* with sac leads to a lower temperature (lower $\delta^{18}\text{O}$) and lower pH (lower $\delta^{11}\text{B}$) reconstruction^{33,38}. However, two observations support that the presence of the sac-like final chamber does not alter either the mean calcification depth estimate of *T. sacculifer* or the pCO_2 estimate of upper-thermocline seawater in the WEP (see Supplementary Text, for more thorough discussion). First, *T. sacculifer* with a sac-like final chamber in core KR05-15 PC01 carries an identical environmental signal (that is Mg/Ca and $\delta^{18}\text{O}$) to those without sac collected from a nearby sediment core that has an excellent preservation of foraminifera shells (MD97-2138; Fig. 1, Supplementary Fig. S6)²⁹. Second, $\delta^{11}\text{B}$ values of *G. sacculifer* from core KR05-15 PC01 are consistent with those from core-top material from the Ontong Java Plateau which is not affected by dissolution¹⁴ (Fig. 1,

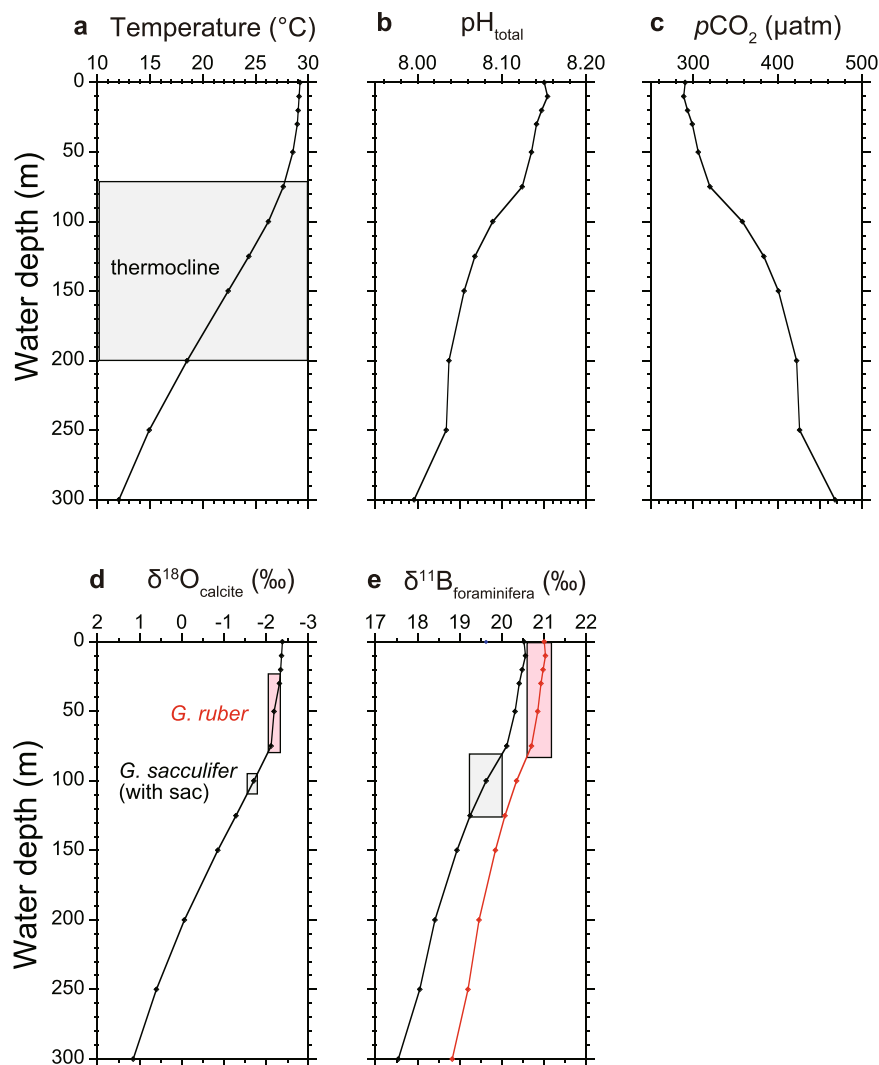


Figure 3. Depth profile of seawater CO₂ system and calcification depth estimation of planktonic foraminifera. Depth profile of seawater properties and calcification depth estimation of *G. ruber*, and *T. sacculifer* (with sac-like final chamber), in the WEP. (a) Depth profile of water temperature⁷⁴. The shaded area indicates thermocline depth. (b) Seawater pH and (c) seawater *p*CO₂ calculated using pre-industrial dissolved inorganic carbon and total alkalinity⁴³. (d) δ¹⁸O and (e) δ¹¹B values estimated using water temperature, salinity, seawater pH, and species-specific δ¹¹B–pH calibration equations.

Supplementary Fig. S7). Thus we conclude that relatively deeper calcification depth is due to location-specific habitat depth preferences of *T. sacculifer*, not due to dissolution effects. The reason of this is likely that the modest sedimentation rate of KR05-15 PC01 (4.5 cm/ky) enabled the fine preservation of foraminifera shells, even though the bottom water was undersaturated. It is also noteworthy that large *T. sacculifer* individuals are less influenced by dissolution, because of a relative proportion of sac versus other chambers are smaller in large individuals³⁸. It is likely that dissolution effects is negligible through the record, because there are little variation in saturation state in the Pacific deep-water in glacial-interglacial timescales³⁹. We also found that the selection of different Mg/Ca–water temperature relationships and consideration of an effect of partial dissolution of *G. ruber* shell^{28,31,40} has a negligible effect on the calculation of surface seawater *p*CO₂ (Supplementary Text, Supplementary Fig. S8). Similarly we found that pH effect on Mg/Ca–water temperature relationships and different total alkalinity estimation scenario since the last glacial period has a negligible effect on the calculation of seawater *p*CO₂ (Supplementary Text, Supplementary Figs S9–S11).

Surface Seawater *p*CO₂

Today (at the reference year 2000 CE), the surface seawater *p*CO₂ of the WEP has a similar value (360 µatm) to the atmospheric value (370 µatm) (Fig. 1)^{41,42}. A CO₂ neutral condition (seawater *p*CO₂ is close to atmospheric *p*CO₂) is also likely to have existed in pre-industrial times when the atmospheric *p*CO₂ value was 280 µatm (ref.³). The *p*CO₂ value of the surface seawater is calculated as 290 µatm (10 µatm higher than the atmospheric value) based on recent instrumental seawater CO₂ system observations made using research vessels and theoretical

calculations considering anthropogenic CO₂ incorporation since pre-industrial times⁴³ (Figs 2c,d and 3c). From the last glacial period to the early Holocene, reconstructed seawater *p*CO₂ values of mixed-layer water obtained using *G. ruber* show variation similar to that of atmospheric values, suggesting that the oceanic surface layer in the WEP remained in a CO₂ neutral condition (Fig. 2c,d). During the mid- Holocene (6.4–8.6 ka), the WEP became a modest source of CO₂ (on average +36 μatm higher than the atmospheric *p*CO₂), which is consistent with modern oceanographic observations (Fig. 2b,c), suggesting that *G. ruber* shells are a reliable recorder of surface seawater CO₂ chemistry. Considering the estimation error of Δ*p*CO₂ (the difference between seawater *p*CO₂ and atmospheric *p*CO₂) from the δ¹¹B value of *G. ruber*, Δ*p*CO₂ was near zero through the last deglaciation (Fig. 2d), showing that there is no evidence of CO₂ release from the WEP during this period. This result is in clear contrast with a previous finding by Palmer and Pearson¹² that the WEP was a CO₂ source region. The reason for this is most likely that *T. sacculifer* (the species used by Palmer and Pearson¹²) record pH and *p*CO₂ values of the upper thermocline, not of the surface water in the WEP. This point is also of great importance for the reconstruction of atmospheric CO₂ using δ¹¹B analysis of *T. sacculifer* shells for the deep past, beyond the limit of Antarctic ice cores (approximately, 800 ka)^{9,15,16,24}, as a deeper calcification depth than the one we assume may result in the overestimation of atmospheric *p*CO₂. We note that previous reconstruction using δ¹¹B of *T. sacculifer* in the marine sediment core collected from the equatorial Atlantic is irrelevant to this issue (see the recent compilation by Dyez *et al.*¹⁵), because their calcification depth is confirmed to lie within mixed layer.

A Linkage Between High and Low Latitude Ocean

During the last glacial period, an efficient biological pump due to iron fertilization and increased stratification of the Southern Ocean due to sea ice expansion around Antarctica resulted in more efficient carbon storage in the deep sea and a drop in the atmospheric *p*CO₂ level^{7,8,44} (Fig. 4). During the last deglaciation, upwelling in the Southern Ocean was enhanced, and carbon was returned to the atmosphere^{8,45,46}. This event was likely accompanied by a stronger connection between the Southern Ocean and surface and thermocline depth of the low-latitude Pacific, which is known as “geochemical tunneling” (Fig. 4). A large variety of geochemical tracers have suggested greater enhancement of water transport due to Ekman pumping by the southward migration of southern westerlies⁷, more aged water mass incorporation into the intermediate water^{6,11,45–47}, and more pronounced primary productivity in the Southern Ocean^{8,48}. Higher surface *p*CO₂ conditions during the last deglaciation reported for the EEP¹⁰ and the CEP (Tahiti)^{11,23} (Fig. 3) were likely a result of these phenomena, as such a water mass was likely accompanied by higher *p*CO₂ water originating from the glacial deep-sea carbon reservoir (Fig. 4). The fact that no high-*p*CO₂ water was observed in the mixed layer of the WEP suggests that the high-*p*CO₂ region expanded southward but not westward (Fig. 4). Our results suggest that throughout deglaciation all of the nutrients/CO₂ upwelled in the EEP were fully utilized by the time these surface waters arrived in the WEP. Additionally, the abovementioned 3-ky precedence of the increase in upper thermocline *p*CO₂ (that is decrease in δ¹¹B) in the WEP at the beginning of the last deglaciation (recorded in *T. sacculifer* shells) relative to the increase in surface *p*CO₂ (recorded in *G. ruber* shells) was likely a result of an early arrival of high *p*CO₂ water to the upper thermocline at approximately 19 ka. A possible source of such water mass is the Southern Ocean, especially via water transport via the Subantarctic Mode Water (SAMW) and Equatorial Undercurrent (Fig. 4). Considering that atmospheric CO₂ began to increase only after about 17.5 ka, as determined from Antarctic ice core records (Fig. 2d), a stronger upwelling condition in the Southern Ocean and subsequent incorporation of high-*p*CO₂ water into the SAMW might have started at 19 ka, although it was not enough to fuel atmospheric CO₂. This idea is partly supported by the EEP surface ocean records at 19 ka that show significantly higher *p*CO₂ than in the atmosphere (i.e., positive Δ*p*CO₂)¹⁰ (Fig. 3). Another important observation is that surface ocean *p*CO₂ in the EEP and the CEP and subsurface *p*CO₂ in the WEP was remained high although atmospheric *p*CO₂ did not increase during the Bølling-Allerød warm interval (B/A; 14.6–12.9 ka). Surface *p*CO₂ reconstruction using δ¹¹B of planktonic foraminifera, *Neogloboquadrina pachyderma*, collected from marine sediment core in the North Pacific (51.27°N, 167.73°E)⁴⁹ shows similar variation to our subsurface *p*CO₂ record, which may provide a hint to understand the mechanism behind, because there is another path that transport nutrient and carbon from the North Pacific to the equatorial Pacific via North Pacific Intermediate Water (NPIW)⁵⁰. It is noteworthy that at the onset of the B/A interval, a collapse of NPIW formation is suggested⁴⁹, which occurred at the same time of a reduction of the southern-sourced water contribution in the thermocline depth of the equatorial Pacific⁵. A hypothesis that *p*CO₂ variability of thermocline in the equatorial Pacific is driven by both north and south high-latitude ocean processes merits testing by obtaining more high-resolution records from wider spatial coverage. In addition, other important research topics include investigating lower-thermocline conditions by utilizing thermocline-dwelling foraminifera shells (e.g., refs^{5,28}) and investigating seawater *p*CO₂ conditions during other glacial terminations, such as the penultimate deglaciation. For these purposes, the boron isotope proxy is a promising tool to create a *p*CO₂ map in order to better understand the redistribution of CO₂ between seawater and the atmosphere during glacial–interglacial cycles. Given a large surface area and its connectivity to the deep ocean, the Southern Ocean most likely had a central role in deglacial CO₂ release into the atmosphere, but relative importance of CO₂ flux from the Southern Ocean and that from other oceanic regions including the equatorial Pacific remains unquantified.

Materials and Methods

Geochemical analyses. We analyzed a marine sediment core obtained from the West Caroline Basin (0.10°S 139.58°E) in 2005 by R/V Kairei. A 15-m-long sediment core that covers the last 400 ka was obtained using a piston coring system (core KR05-15 PC01)²⁶. The top 1.5 m of the core was used for this study, as it covers the time period since the last glacial period. Sediment lithologies are foraminifera-rich clay (brown) for the top 30 cm and clay with foraminifera (greenish gray) from a depth of 30 cm to 150 cm. The archive half was cut in 2 cm intervals, and the sediment samples were gently washed under running water over a 63 μm sieve and dried

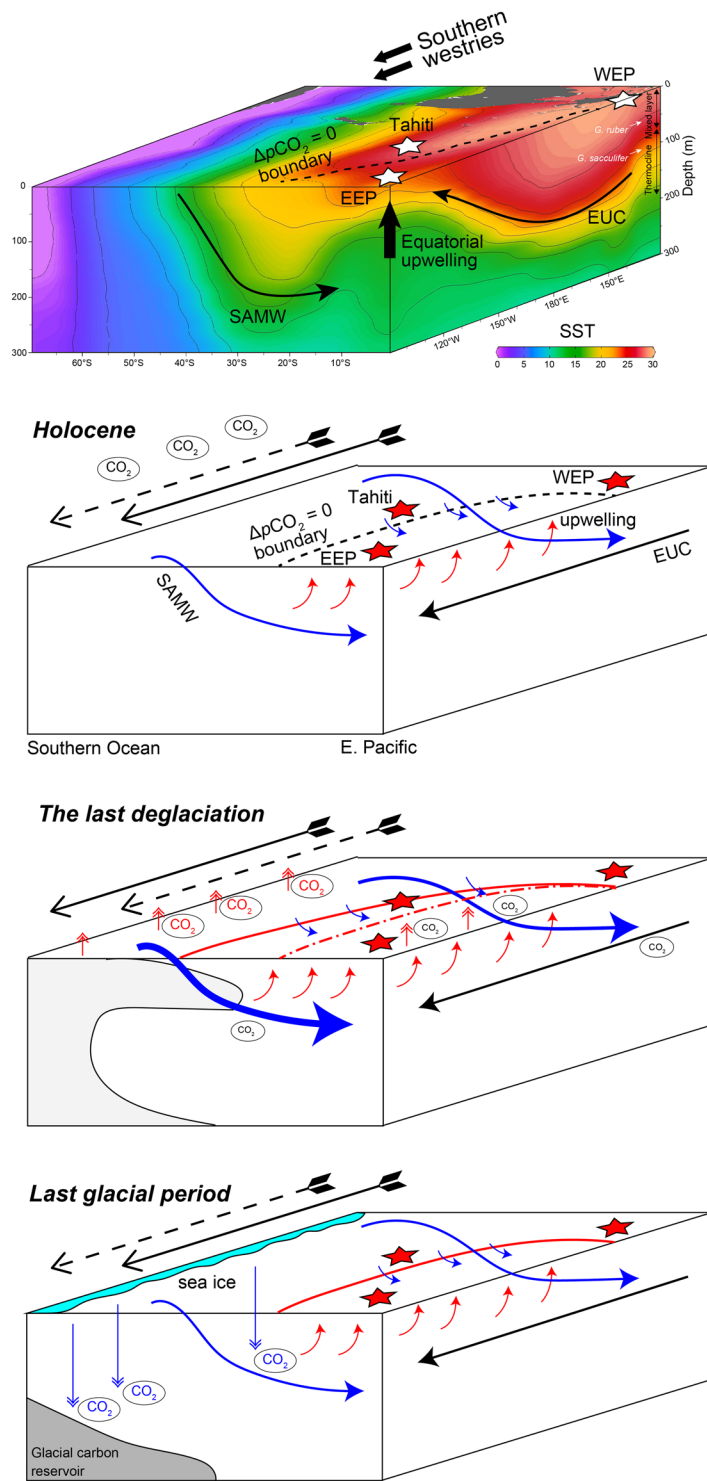


Figure 4. Schematics of deglacial marine carbon cycles. Schematics of carbon cycles and climatology in the South Pacific Ocean for three time periods: the last glacial period, the last deglaciation, and the Holocene.

at 60 °C in an oven. The sieved materials were further divided into size fractions of 63–255, 255–300, 300–355, 355–425, 425–500, and 500–850 μm , and stored in plastic vials.

The age model of the sediment core was established by 17 radiocarbon dates measured by accelerator mass spectrometry (AMS). If enough calcium carbonate materials were available, shells of mono-specific planktonic foraminifera (*T. sacculifer*) were used; otherwise, shells of mixed planktonic foraminifera were used (Supplementary Table S1). Seven samples were submitted as carbonate to the National Ocean Sciences Accelerator Mass Spectrometry Facility (NOSAMS), Woods Hole Oceanographic Institution (WHOI), and the remaining samples were analyzed in the Atmosphere and Ocean Research Institute (AORI), University of Tokyo. Three of the

20 samples were omitted as they showed anomalous values compared with neighboring data. Conventional ^{14}C ages were converted into calendar age before 1950 CE using a Marine13 calibration curve⁵¹ with a local marine ^{14}C reservoir age of 40 ± 21 years^{52,53} (Supplementary Fig. S1).

More than two shells of *Uvigerina* spp. were hand-picked under a microscope from the sediment samples from size fractions of 300–355 and 355–425 μm . Shells of *G. ruber* (white, s.s./s.l.) and *T. sacculifer* (with a sac-like final chamber) were hand-picked under microscope from size fractions of 300–355 and 500–850 μm , respectively. All samples were weighed, and if the sample amount was insufficient for the subsequent geochemical analysis, some continuous samples were mixed (at most eight samples).

Oxygen isotopes of benthic foraminifera *Uvigerina* spp. were measured using an isotope-ratio mass spectrometer (Isoprime) with an automated carbonate reaction system (Multiprep) installed at Kochi Core Center (KCC), Japan. The values of $\delta^{18}\text{O}$ are reported with respect to the Vienna Pee Dee Belemnite standard using standard delta notation in permil⁵⁴. Analytical precision for long-term measurement of the calcite standard (IAEA603) was better than 0.1‰. A drift correction for the sample $\delta^{18}\text{O}$ values was performed, as the long-term drift of the measured IAEA603 values of the standards during the measurement period between June 2017 and June 2018 was observed to be 0.12–0.32‰ isotopically heavier than the certified value of -2.37 ‰ (IAEA Reference Products; available at http://nucleus.iaea.org/rpst/ReferenceProducts/ReferenceMaterials/Stable_Isotopes/index.htm).

A technique for measuring Mg/Ca, $\delta^{18}\text{O}$, and $\delta^{11}\text{B}$ from the same planktonic foraminifera sample was established in this study (Supplementary Fig. S2). The foraminifera cleaning methodology was after Baker *et al.*⁵⁵. Weighed samples were crushed gently between two acrylic slides until the insides of all the chambers were visible under stereoscopic microscope. Samples were subsequently transferred to 1.5 mL Eppendorf tubes. Samples were sonicated five times with Milli-Q water and twice with methanol. The supernatant containing suspended fine grains was removed immediately from the sample after ultrasonication. To remove organic matter by oxidation, 0.1 N NaOH buffered 30% H_2O_2 was added and heated at 80 °C for 10 min. Subsequent reductive steps were skipped, as they do not have a discernible effect on $\delta^{11}\text{B}$ measurement^{33,56}.

Several hundred micrograms of samples were divided for $\delta^{18}\text{O}$ measurements using the Isoprime spectrometer (Supplementary Fig. S2). The methodology of $\delta^{18}\text{O}$ measurements was the same as above. The remaining samples were transferred to acid-cleaned Teflon vials. After weak acid-leaching of any adhesive materials attached to calcium carbonate, 1–2 mL 0.1 M HCl was added to the samples until complete dissolution, together with 5 μL of 1% mannitol solution. A total of 30 μL of sample was taken from the solution and diluted with 5 mL of 0.15 M HNO_3 with internal standards (50 ppb Be and 100 ppb Sc, Y, and In). First, Ca concentration was measured using a quadrupole inductively coupled plasma mass spectrometer (Q-ICPMS; Agilent7700, Agilent Technology) installed at KCC (Supplementary Fig. S2). Then, 30 μL of sample was taken again from the solution and diluted to make the Ca concentration of each sample 10 ppm (matrix matching). Matrix matching is essential for the precise determination of trace element/Ca ratios^{28,57}. Standard solution (200 ppb of Mg and Sr, 50 ppb of B, Al, Mn, Rb, and Ba) was prepared by diluting commercially available 1000 $\mu\text{g/g}$ single element standards with the abovementioned 0.15 M HNO_3 containing internal standards. Elemental ratios of samples were determined using the Agilent7700 instrument, with a machine drift correction. A calcium carbonate standard JCp-1, provided by the Geological Survey of Japan, was repeatedly analyzed to calculate the precision of the trace element/Ca ratio measurements. The precision of Mg/Ca analysis was 3.4% (1σ).

Boron isotopic measurements were conducted following the methodology of Tanimizu *et al.*⁵⁸. Briefly, the boron was purified using cation- and anion-exchange resin columns, and the samples were dissolved with an acid mixture composed of 0.15 M HNO_3 , 0.05 M HF, and 0.1% mannitol to obtain a solution of 20–50 ppb B. Li standard ($^7\text{Li}/^6\text{Li}$ isotopic reference) was added to each sample to correct a mass discrimination. $\delta^{11}\text{B}$ values were determined with a multi-collector inductively coupled plasma mass spectrometer (MC-ICPMS) (Neptune, Thermo Finnigan) installed at KCC, against the isotopic reference NIST-SRM 951, using a standard-sample bracketing technique under wet plasma conditions. Since July 2017, a jet sampling cone instead of a normal sampling cone has been used with an X skimmer cone, which significantly increased beam intensity for both carbonate standard JCp-1 and seawater standard AE122 (Supplementary Fig. S3). $\delta^{11}\text{B}$ values of JCp-1 were determined with different boron concentrations (10, 20, 30, 40, 50, and 75 ppb), which yielded consistent values with a mean of 24.38 ± 0.28 ‰ (2σ , $n = 37$) only if ^{11}B beam intensity was greater than 0.2 V (Supplementary Fig. S3); in the case of beam intensity of less than 0.2 V, analytical error increased to ± 0.5 ‰ (2σ , $n = 10$). $\delta^{11}\text{B}$ values of AE122 were determined with a uniform concentration of 75 ppb, which yielded a mean value of 39.48 ± 0.24 ‰ (2σ , $n = 14$). As with JCp-1, the measurement of AE122 using a jet sampling cone resulted in higher beam intensity than measurement using a normal cone, and there were no discernible differences in $\delta^{11}\text{B}$ between selections of sampling cones (Supplementary Fig. S3). $\delta^{11}\text{B}$ values of both JCp-1 and AE122 were within the previously published 2σ range of data compiled from different laboratories by Foster *et al.*¹⁸ and Foster *et al.*⁵⁹. The analytical error of JCp-1 (± 0.14 ‰, 1σ) was taken as the analytical errors of the foraminifera samples, except when ^{11}B beam intensity was less than 0.2 V, in which case the larger error (± 0.25 ‰, 1σ) was employed.

To assess the reproducibility of the methodology, Mg/Ca, $\delta^{18}\text{O}$, and $\delta^{11}\text{B}$ of *T. sacculifer* samples in the Holocene section were measured 2–4 times, as they were abundant in this interval. The results of the Mg/Ca, $\delta^{18}\text{O}$, and $\delta^{11}\text{B}$ replicates showed good agreement within the estimated analytical errors (Supplementary Fig. S4), supporting the reproducibility of this methodology.

Age model. To obtain age-depth model of the sediment core KR05-15 PC01 in 1 cm intervals from 17 radiocarbon dates we used a recently published age-depth modeling tool “Undatable” (ref.²⁷), which uses a deterministic approach with a positive sediment accumulation rate (Supplementary Fig. S1). We confirmed the robustness of the age model by comparing the $\delta^{18}\text{O}$ values of *Uvigerina* spp. from core KR05-15 PC01 with a benthic $\delta^{18}\text{O}$ record for Pacific deep-sea sediment⁶⁰ (Supplementary Fig. S1). The values are in good agreement in the glacial period (30–18 ka), but there is an offset thereafter (maximum difference of 0.7‰). Although the absolute $\delta^{18}\text{O}$

values are different, the shapes of the “up-down” patterns during 10–7 ka show excellent agreement. We infer that the difference is likely due to a regional difference in bottom-water temperature.

Data screening. Some $\delta^{11}\text{B}$ data from planktonic foraminifera that showed anomalously low values (1–2‰) were discarded from the calculation of $p\text{CO}_2$. Such data were accompanied by higher Mg/Ca ratios (by more than 0.3 mmol/mol) as well as high Al counts (typically more than 50,000 cps), suggesting that boron was contaminated by silicate in the sediment^{55,61}. Barker *et al.*⁵⁵ investigated how the Mg/Ca ratio of foraminifera shells changes according to physical and chemical cleaning steps, and clearly showed that high Mg/Ca ratios result from insufficient removal of silicate (which is a major component of marine sediment). Similarly, without cleaning, the Al/Ca ratio varies in concert with the Mg/Ca ratio of foraminifera⁵⁵, suggesting that Mg/Ca and Al content are useful to identify contaminated samples. As foraminifera shells were dissolved in 0.1 M HCl, excess boron likely originated from some material that is reactive with HCl. Ishikawa and Nakamura⁶¹ reported that the $\delta^{11}\text{B}$ value of the HCl-soluble fraction of subtropical North Pacific marine sediment (nanno ooze; DSDP313 1–5; 20°N 170°W) was 8.0‰ with a significant boron abundance (15 ppm), which is much lower than $\delta^{11}\text{B}$ values of *G. ruber* (20–22‰) and *T. sacculifer* (19–21‰). Thus, we infer that the anomalously low foraminiferal $\delta^{11}\text{B}$ values observed in this study can be explained by contamination by boron that was not removed sufficiently during the cleaning steps.

Calculation of pH and $p\text{CO}_2$. Water temperature and salinity need to be known for the calculation of seawater pH from the measured $\delta^{11}\text{B}$ of foraminifera shells. Mg/Ca ratios of foraminifera shells were used for the calculation. The Mg/Ca–T equation of Sagawa *et al.*²⁸ was used, as this equation was established by using a marine sediment core collected from a similar depth and location in the WEP (3cBX, 8.02°N, 139.64°E, 2829 m, Fig. 1).

$$T = 1/0.077 * \ln(\text{Mg/Ca}/0.455)$$

where T is temperature in degrees Celsius.

Seawater $\delta^{18}\text{O}$ ($\delta^{18}\text{O}_{\text{SW}}$) was used to calculate salinity, as there is a linear relationship between salinity and $\delta^{18}\text{O}_{\text{SW}}$. The $\delta^{18}\text{O}$ of foraminifera calcite is a function of temperature and $\delta^{18}\text{O}_{\text{SW}}$ (ref.⁶²), so $\delta^{18}\text{O}_{\text{SW}}$ can be calculated from $\delta^{18}\text{O}$ and temperature (from Mg/Ca).

$$10^3 * \ln \alpha = 18.03 * 10^3 / (T + 273.13) - 32.42$$

or

$$T = 16.1 - 4.64 * (\delta^{18}\text{O}_{\text{calcite}} - \delta^{18}\text{O}_{\text{SW}}) + 0.09 * (\delta^{18}\text{O}_{\text{calcite}} - \delta^{18}\text{O}_{\text{SW}})^2$$

Here, α is the fractionation factor and T is temperature in degrees Celsius (after ref.⁶³). However, in glacial–interglacial timescales, past $\delta^{18}\text{O}_{\text{SW}}$ changes need to be further considered for the calculation. Since the last glacial period, enormous volumes of freshwater with isotopically lighter $\delta^{18}\text{O}$ values previously stored in continental ice sheets have entered the ocean, making global seawater $\delta^{18}\text{O}$ lighter by ~1‰ (ice volume effect); as an additional consequence, sea level rose by ~135 m. As ice-derived $\delta^{18}\text{O}_{\text{SW}}$ change has a linear relationship with global sea level, we estimated the ice volume effect from the reconstructed sea level curve of Yokoyama *et al.*⁶⁴. We assume that a sea level change of 135 m causes a 1‰ change in $\delta^{18}\text{O}_{\text{SW}}$ (ref.⁶⁵). The ice volume-corrected $\delta^{18}\text{O}_{\text{SW}}$ values were subsequently used for the calculation of salinity using the reported equation of Schmidt⁶⁶:

$$S = 0.422 * \delta^{18}\text{O}_{\text{SW(ice-volume-corrected)}} - 14.379$$

where S is salinity. There are known offsets between the theoretically expected $\delta^{11}\text{B}$ of borate ions in the seawater ($\delta^{11}\text{B}_{\text{borate}}$) and the measured $\delta^{11}\text{B}$ of foraminifera calcite ($\delta^{11}\text{B}_{\text{borate}}$), and these relationships differ among species (e.g., ref.¹³). For the calculation of seawater pH, the empirical relationships of Marinez-Boti *et al.*⁶⁷ and Henehan *et al.*²³ were used for *G. ruber* and *T. sacculifer*, respectively. Finally, seawater pH was obtained by the following theoretical equation:

$$\text{pH} = \text{p}K_{\text{B}} - \log((\delta^{11}\text{B}_{\text{SW}} - \delta^{11}\text{B}_{\text{borate}})/(\alpha * \delta^{11}\text{B}_{\text{borate}} - \delta^{11}\text{B}_{\text{SW}} * 10^3 * (\alpha - 1)))$$

where $\text{p}K_{\text{B}}$ is the dissociation constant of boric acid and is a function of temperature and salinity (and pressure)⁶⁸, $\delta^{11}\text{B}_{\text{SW}}$ is the $\delta^{11}\text{B}$ value of seawater, which is constant on glacial–interglacial timescales⁵⁹, and α is the fractionation factor between borate ions and boric acid in the seawater^{69,70}.

For the calculation of seawater $p\text{CO}_2$, both pH and one more CO_2 system parameter need to be known. In this study, the total alkalinity (TA) of the seawater was used for the calculation, and was estimated using a multiple regression equation (a function of temperature and salinity) reported by Lee *et al.*⁷¹. The *CO2calc* software (version 4.0.9), provided by the U.S. Geological Survey (available at <https://www.usgs.gov/software/co2calc>), was used to calculate $p\text{CO}_2$ from pH, TA, temperature, and salinity. Dissociation constants for K_1 and K_2 from Lueker *et al.*⁷² and for K_{B} from Dickson⁶⁸ were used. $\Delta p\text{CO}_2$ (seawater $p\text{CO}_2$ minus atmospheric $p\text{CO}_2$) was calculated from the obtained seawater $p\text{CO}_2$ using contemporary atmospheric $p\text{CO}_2$ reconstructed from Antarctic ice cores^{1–3}.

Estimated calcification depth of planktonic foraminifera. Calcification depths of *G. ruber* and *T. sacculifer* were estimated by comparing theoretically predicted depth profiles of $\delta^{18}\text{O}$ and $\delta^{11}\text{B}$ and measured $\delta^{18}\text{O}$ and $\delta^{11}\text{B}$ values in the Holocene section. For the calculation, depth profiles of annual temperature and salinity from the World Ocean Atlas (data available at <https://odv.awi.de/data/ocean/world-ocean-atlas-2009/>) were used (Fig. 3a). For CO_2 system variables, gridded data of dissolved inorganic carbon (DIC) and TA from Global Ocean

Data Analysis Project (GLODAP; data available at <https://odv.awi.de/data/ocean/glodap-gridded-data/>)⁴³ were used. Anthropogenic DIC incorporation after the industrial revolution was subtracted from DIC data to estimate pre-industrial DIC, and then all CO₂ system variables in the pre-industrial era were calculated using the *CO2calc* software (Fig. 3b,c). The theoretical $\delta^{18}\text{O}$ depth profile of calcite was calculated from temperature and $\delta^{18}\text{O}_{\text{SW}}$ values obtained from NASA GISS (data available at http://iridl.ldeo.columbia.edu/SOURCES/NASA/GISS/LeGrande_Schmidt2006/v1p1/). As foraminifera calcite is precipitated in isotopic equilibrium with the ambient seawater, the $\delta^{18}\text{O}$ depth profile of inorganic calcite represents that of foraminifera calcite (Fig. 3d). The $\delta^{11}\text{B}$ depth profile of foraminifera calcite can be predicted from the known temperature, salinity, and pH, as well as an empirical relationship between the $\delta^{11}\text{B}$ of seawater borate ion and that of *G. ruber*⁶⁷ and *T. sacculifer*⁴³ (Fig. 3e). As the empirical relationship differs among foraminifera species, depth profiles of the predicted $\delta^{11}\text{B}$ of foraminifera shells differ between *G. ruber* and *T. sacculifer* (Fig. 3e). The estimated calcification depths are 0–75 m (within the mixed layer) and 75–125 m (below the mixed layer; upper thermocline) for *G. ruber* and *T. sacculifer*, respectively.

Monte Carlo simulation. As many variables are required to calculate pH, $p\text{CO}_2$, and $\Delta p\text{CO}_2$, Monte Carlo simulation is useful to calculate the estimation errors of these outputs considering all involved errors. All calculations were performed using the freeware *R* (version 3.0; available at: <https://www.r-project.org>) with the *seacarb* (v.3.2.8) package for seawater CO₂ chemistry calculation⁷³. The same dissociation constants (K_1 , K_2 , and K_B) that were used for the seawater CO₂ chemistry calculation using the *CO2calc* software were employed. Analytical errors (1σ) of Mg/Ca (3%), $\delta^{18}\text{O}$ (0.1‰), and $\delta^{11}\text{B}$ (0.14‰ and 0.25‰ when ¹¹B beam intensity was greater than 0.2 V and less than 0.2 V, respectively) were considered. Estimation errors of atmospheric $p\text{CO}_2$ (2 μatm) reconstructed from Antarctic ice core were also considered. Variables were randomly changed in which errors are normally distributed (mean \pm error), and the calculation was repeated 1000 times. Standard deviations of 1000 outputs of pH, $p\text{CO}_2$, and $\Delta p\text{CO}_2$ were then calculated, and were regarded as estimation errors (Fig. 2b–d). The error ranged from 0.014 to 0.030 for pH, and from 9 to 32 μatm for both $p\text{CO}_2$ and $\Delta p\text{CO}_2$.

References

- Marcott, S. A. *et al.* Centennial-scale changes in the global carbon cycle during the last deglaciation. *Nature* **514**, 616–619 (2014).
- Ahn, J. & Brook, E. J. Siple Dome ice reveals two modes of millennial CO₂ change during the last ice age. *Nat. Commun.* <https://doi.org/10.1038/ncomms4723> (2014).
- Lüthi, D. *et al.* High-resolution carbon dioxide concentration record 650,000–800,000 years before present. *Nature* **453**, 379–382 (2008).
- Basak, C. *et al.* Breakup of last glacial deep stratification in the South. *Pacific. Science* **359**, 900–904 (2018).
- Pena, L. D. *et al.* Rapid changes in meridional advection of Southern Ocean intermediate waters to the tropical Pacific during the last 30 kyr. *Earth Planet. Sci. Lett.* **368**, 20–32 (2013).
- Skinner, L. C., Fallon, S., Waelbroeck, C., Michel, E. & Barker, S. Ventilation of the Deep Southern Ocean and Deglacial CO₂ Rise. *Science* **328**, 1147–1151 (2010).
- Sigman, D. M., Hain, M. P. & Haug, G. H. The polar ocean and glacial cycles in atmospheric CO₂ concentration. *Nature* **466**, 47–55 (2010).
- Anderson, R. F. *et al.* Wind-Driven Upwelling in the Southern Ocean and the Deglacial Rise in Atmospheric CO₂. *Science* **323**, 1443–1448 (2009).
- Foster, G. L. & Rae, J. W. B. Reconstructing Ocean pH with Boron Isotopes in Foraminifera. *Annu. Rev. Earth Planet. Sci.* **44**, 207–37 (2016).
- Martinez-Boti, M. A. *et al.* Boron isotope evidence for oceanic carbon dioxide leakage during the last deglaciation. *Nature* **518**, 219–222 (2015).
- Kubota, K., Yokoyama, Y., Ishikawa, T., Obrochta, S. & Suzuki, A. Larger CO₂ source at the equatorial Pacific during the last deglaciation. *Sci. Rep.* <https://doi.org/10.1038/srep05261> (2014).
- Palmer, M. R. & Pearson, P. N. A 23,000-Year Record of Surface Water pH and $p\text{CO}_2$ in the Western Equatorial Pacific. *Ocean. Science* **300**, 480–482 (2003).
- Henehan, M. J. *et al.* A new boron isotope-pH calibration for *Orbulina universa*, with implications for understanding and accounting for 'vital effects'. *Earth Planet. Sci. Lett.* **454**, 282–292 (2016).
- Foster, G. L. Seawater pH, $p\text{CO}_2$ and $[\text{CO}_3^{2-}]$ variations in the Caribbean Sea over the last 130 kyr: A boron isotope and B/Ca study of planktic foraminifera. *Earth Planet. Sci. Lett.* **271**, 254–266 (2008).
- Dyez, K. A., Hönisch, B. & Schmidt, G. A. Early Pleistocene obliquity-scale $p\text{CO}_2$ variability at ~1.5 million years ago. *Paleoceanogr. Paleoclimatol.* **33**, 1270–1291 (2018).
- Hemming, N. G. & Hönisch, B. Boron isotopes in marine carbonate sediments and the pH of the ocean. *Dev. Mar. Geol.* **1**, 717–34 (2007).
- Ni, Y., Foster, G. L. & Elliott, T. The accuracy of $\delta^{11}\text{B}$ measurements of foraminifera. *Chem. Geol.* **274**, 187–195 (2010).
- Foster, G. L. *et al.* Interlaboratory comparison of boron isotope analyses of boric acid, seawater and marine CaCO₃ by MC-ICPMS and NTIMS. *Chem. Geol.* **358**, 1–14 (2013).
- Farmer, J. R., Hönisch, B. & Uchikawa, J. Single laboratory comparison of MC-ICP-MS and N-TIMS boron isotope analyses in marine carbonates. *Chem. Geol.* **447**, 173–182 (2016).
- Vengosh, A., Chivas, A. R. & McCulloch, M. T. Direct determination of boron and chlorine isotopic compositions in geological materials by negative thermal-ionization mass spectrometry. *Chem. Geol.* **79**, 333–343 (1989).
- Lecuyer, C., Grandjean, P., Reynard, B., Albarede, F. & Telouk, P. ¹¹B/¹⁰B analysis of geological materials by ICP-MS Plasma 54: application to the boron fractionation between brachiopod calcite and seawater. *Chem. Geol.* **186**, 45–55 (2002).
- Aggarwal, J. K., Sheppard, D., Mezger, K. & Pernicka, E. Precise and accurate determination of boron isotope ratios by multiple collector ICP-MS: origin of boron in the Ngawha geothermal system, New Zealand. *Chem. Geol.* **199**, 31–42 (2003).
- Douville, E. *et al.* Abrupt sea surface pH change at the end of the Younger Dryas in the central sub-equatorial Pacific inferred from boron isotope abundance in corals (*Porites*). *Biogeosciences* **7**, 2445–2459 (2010).
- Chalk, T. B. *et al.* Causes of ice age intensification across the mid-Pleistocene transition. *Proc. Natl Acad. Sci. USA* **114**, 13114–13119 (2017).
- Picaut, J., Ioualalen, M., Menkes, C., Delcroix, T. & McPhaden, M. J. Mechanism of the Zonal displacements of the Pacific warm pool: implications for ENSO. *Science* **274**, 1486–1489 (1996).
- Yamazaki, T., Kanamatsu, T., Mizuno, S., Hokanishi, N. & Gaffar, E. Z. Geomagnetic field variations during the last 400 kyr in the western equatorial Pacific: Paleointensity-inclination correlation revisited. *Geophys. Res. Lett.* **35**, L20307, <https://doi.org/10.1029/2008GL035373> (2008).

27. Lougheed, B. C. & Obrochta, S. P. A rapid, deterministic age-depth modeling routine for geological sequences with inherent depth uncertainty. *Paleoceanogr. Paleoclimatol.* **34**, 122–133 (2019).
28. Sagawa, T., Yokoyama, Y., Ikehara, M. & Kuwae, M. Shoaling of the western equatorial Pacific thermocline during the last glacial maximum inferred from multispecies temperature reconstruction of planktonic foraminifera. *Palaeogeogr. Palaeoclim. Palaeoecol.* **346–347**, 120–129 (2012).
29. de Garidel-Thoron, T. *et al.* A multiproxy assessment of the western equatorial Pacific hydrography during the last 30 kyr. *Paleoceanogr.* **22**, PA3204, <https://doi.org/10.1029/2006PA001269> (2007).
30. Rippert, N. *et al.* Constraining foraminiferal calcification depths in the western Pacific warm pool. *Mar. Micropaleontol.* **128**, 14–27 (2016).
31. Dekens, P. S., Lea, D. W., Pak, D. K. & Spero, H. J. Core top calibration of Mg/Ca in tropical foraminifera: Refining paleotemperature estimation. *Geochem. Geophys. Geosys.* **3**, <https://doi.org/10.1029/2001GC000200> (2002).
32. Fehrenbacher, J. & Martin, P. Western equatorial Pacific deep water carbonate chemistry during the Last Glacial Maximum and deglaciation: Using planktic foraminiferal Mg/Ca to reconstruct sea surface temperature and seafloor dissolution. *Paleoceanography* **26**, PA2225, <https://doi.org/10.1029/2010PA002035> (2011).
33. Ni, Y. *et al.* A core top assessment of proxies for the ocean carbonate system in surface-dwelling foraminifers. *Paleoceanography* **22**, PA3212, <https://doi.org/10.1029/2006PA001337> (2007).
34. Bijma, J. & Hemleben, C. Population dynamics of the planktic foraminifer *Globigerinoides sacculifer* (Brady) from the central Red Sea. *Deep-Sea Res., Part 1, Oceanogr. Res. Pap.* **41**, 485–510 (1994).
35. Erez, J., Almogi-Labin, A. & Avraham, S. On the life history of planktonic foraminifera: lunar reproduction cycle in *Globigerinoides sacculifer* (Brady). *Paleoceanography* **6**, 295–306 (1991).
36. Be, A. W. H. Gametogenic calcification in a spinose planktonic foraminifer, *Globigerinoides sacculifer* (Brady). *Mar. Micropaleontol.* **5**, 283–310 (1980).
37. Rebotim, A. *et al.* Factors controlling the depth habitat of planktonic foraminifera in the subtropical eastern North Atlantic. *Biogeosciences* **14**, 827–859 (2017).
38. Hönisch, B. & Hemming, N. G. Ground-truthing the boron isotope-paleo-pH proxy in planktonic foraminifera shells: Partial dissolution and shell size effects. *Paleoceanography* **19**, PA4010, <https://doi.org/10.1029/2004PA001026> (2004).
39. Yu, J. *et al.* Loss of carbon from the deep sea since the Last Glacial Maximum. *Science* **330**, 1084–1087 (2010).
40. Rosenthal, Y. & Lohmann, G. P. Accurate estimation of sea surface temperatures using dissolution-corrected calibrations for Mg/Ca paleothermometry. *Paleoceanography* **17**, 1044, <https://doi.org/10.1029/2001PA000749> (2002).
41. Midorikawa, T. *et al.* Y. Decreasing pH trend estimated from 25-yr time series of carbonate parameters in the western North Pacific. *Tellus* **62B**, 649–659 (2010).
42. Takahashi, T. *et al.* Climatological mean and decadal change in surface ocean pCO₂, and net sea–air CO₂ flux over the global oceans. *Deep-Sea Res.* **56**, 554–577 (2009).
43. Key, R. M. *et al.* A global ocean carbon climatology: Results from Global Data Analysis Project (GLODAP). *Global Biogeochem. Cy.*, <https://doi.org/10.1029/2004GB002247> (2004).
44. Jaccard, S. L., Galbraith, E. D., Martínez-García, A. & Anderson, R. F. Covariation of deep Southern Ocean oxygenation and atmospheric CO₂ through the last ice age. *Nature* **530**, 207–210 (2016).
45. Marchitto, T. M., Lehman, S. J., Ortiz, J. D., Flückiger, J. & van Geen, A. Marine Radiocarbon Evidence for the Mechanism of Deglacial Atmospheric CO₂ Rise. *Science* **316**, 1456–1459 (2007).
46. Ronge, T. A. *et al.* Radiocarbon constraints on the extent and evolution of the South Pacific glacial carbon pool. *Nat. Commun.* **7**:11487, <https://doi.org/10.1038/ncomms11487>.
47. Basak, C., Martin, E. E., Horikawa, K. & Marchitto, T. M. Southern Ocean source of ¹⁴C-depleted carbon in the North Pacific Ocean during the last deglaciation. *Nat. Geosci.* **3**, 770–773 (2010).
48. Horn, M. G., Beucher, C. P., Robinson, R. S. & Brzezinski, M. A. Southern ocean nitrogen and silicon dynamics during the last deglaciation. *Earth Planet. Sci. Lett.* **310**, 334–339 (2011).
49. Gray, W. R. *et al.* Deglacial upwelling, productivity and CO₂ outgassing in the North Pacific Ocean. *Nat. Geosci.* **11**, 340–344 (2018).
50. Sarmiento, J. Á., Gruber, N., Brzezinski, M. A. & Dunne, J. P. High-latitude controls of thermocline nutrients and low latitude biological productivity. *Nature* **427**, 56–60 (2004).
51. Reimer, P. J. *et al.* IntCal13 and Marine13 radiocarbon age calibration curves 0–50,000 years cal BP. *Radiocarbon* **55**, 1869–1887 (2013).
52. Petchey, F. & Ulm, S. Marine Reservoir Variation in the Bismarck Region: An Evaluation of Spatial and Temporal Change in ΔR and R Over the Last 3000 Years. *Radiocarbon* **54**, 45–58 (2012).
53. McGregor, H. V., Gagan, M. K., McCulloch, M. T., Hodge, E. & Mortimer, G. Mid-Holocene variability in the marine 14C reservoir age for northern coastal Papua New Guinea. *Quat. Geochron.* **3**, 213–225 (2008).
54. Craig, H. Isotopic standards for carbon and oxygen and correction factors for mass-spectrometric analysis of carbon dioxide. *Geochim. Cosmochim. Acta* **12**, 133–149 (1957).
55. Barker, S., Greaves, M. & Elderfield, H. A study of cleaning procedures used for foraminiferal Mg/Ca paleothermometry. *Geochem. Geophys. Geosys.* **4**, <https://doi.org/10.1029/2003GC000559> (2003).
56. Misra, S., Owen, R., Kerr, J., Greaves, M. & Elderfield, H. Determination of δ¹¹B by HR- ICP-MS from mass limited samples: application to natural carbonates and water samples. *Geochim. Cosmochim. Acta* **140**, 531–552 (2014).
57. de Villiers, S., Greaves, M. & Elderfield, H. An intensity ratio calibration method for the accurate determination of Mg/Ca and Sr/Ca of marine carbonates by ICP-AES. *Geochem. Geophys. Geosys.* **3**, 1001, <https://doi.org/10.1029/2001GC000169> (2002).
58. Tanimizu, M., Nagaishi, K. & Ishikawa, T. A Rapid and Precise Determination of Boron Isotope Ratio in Water and Carbonate Samples by Multiple Collector ICP-MS. *Anal. Sci.* **34**, 667–674 (2018).
59. Foster, G. L., Pogge von Strandmann, P. A. E. & Rae, J. W. B. Boron and magnesium isotopic composition of seawater. *Geochem. Geophys. Geosys.* **11**, Q08015 (2010).
60. Lisiecki, L. E. & Raymo, M. E. Diachronous benthic δ¹⁸O responses during late Pleistocene terminations. *Paleoceanography* **24**, PA3210 (2009).
61. Ishikawa, T. & Nakamura, E. Boron isotope systematics of marine sediments. *Earth Planet. Sci. Lett.* **117**, 567–580 (1993).
62. Kim, S.-T. & O’Neil, J. R. Equilibrium and nonequilibrium oxygen isotope effects in synthetic carbonates. *Geochim. Cosmochim. Acta* **61**, 3461–3475 (1997).
63. Bemis, B. E., Spero, H. J., Bijma, J. & Lea, D. W. Reevaluation of the oxygen isotopic composition of planktonic foraminifera: Experimental results and revised paleotemperature equations. *Paleoceanography* **13**, 150–160 (1998).
64. Yokoyama, Y. *et al.* Rapid glaciation and a two-step sea level plunge into the Last Glacial Maximum. *Nature* **559**, 603–607 (2018).
65. Adkins, J. F., McIntyre, K. & Schrag, D. P. The Salinity, Temperature, and δ¹⁸O of the Glacial Deep. *Ocean. Science* **298**, 1769–1773 (2002).
66. Schmidt, G. A. Error analysis of paleo-salinity calculations. *Paleoceanography* **14**, 422–429 (1999).
67. Martínez-Boti, M. A. *et al.* Plio-Pleistocene climate sensitivity evaluated using high-resolution CO₂ records. *Nature* **518**, 49–54 (2015).
68. Dickson, A. G. Thermodynamics of the dissociation of boric acid in synthetic seawater from 273.15 to 318.15 K. *Deep-Sea Res.* **37**, 755–766 (1990).

69. Klochko, K., Kaufman, A. J., Yao, W., Byrne, R. H. & Tossell, J. A. Experimental measurement of boron isotope fractionation in seawater. *Earth Planet. Sci. Lett.* **248**, 276–285 (2006).
70. Nir, O., Vengosh, A., Harkness, J. S., Dwyer, G. S. & Lahav, O. Direct measurement of the boron isotope fractionation factor: reducing the uncertainty in reconstructing ocean paleo-pH. *Earth Planet. Sci. Lett.* **414**, 1–5 (2015).
71. Lee, K. *et al.* Global relationships of total alkalinity with salinity and temperature in surface waters of the world's oceans. *Geophys. Res. Lett.* **33**, L19605, <https://doi.org/10.1029/2006GL027207> (2006).
72. Lueker, T. J., Dickson, A. G. & Keeling, C. D. Ocean pCO₂ calculated from dissolved inorganic carbon, alkalinity, and equations for K-1 and K-2: validation based on laboratory measurements of CO₂ in gas and seawater at equilibrium. *Mar. Chem.* **70**, 105–119 (2000).
73. Lavigne, H., Epitalon, J. M. & Gattuso J. P. seacarb: seawater carbonate chemistry with R. R package version 3.0, <http://CRAN.R-project.org/package=seacarb> (2011).
74. Locarnini, R. A. *et al.* World Ocean Atlas 2009, Volume 1: Temperature. S. Levitus, Ed. NOAA Atlas NESDIS 68, US. Government Printing Office, Washington, D.C., 184 pp. (2010).

Acknowledgements

We would like to thank N. Ahagon for core curation and assistance in sediment core sampling; H. Takagi for assistance in planktonic foraminifera picking; K. Nagaishi, T. Kawai, Y. Nagaiwa, and N. Asakura for laboratory management and technical support in Mg/Ca and $\delta^{11}\text{B}$ analyses; Y. Fujimura and T. Komatsu for technical support in $\delta^{18}\text{O}$ analysis; and Y. Miyairi, T. Aze, S. Izawa, and Y. Ando for technical support in ^{14}C analyses. We acknowledge that marine sediment core was obtained from JAMSTEC Core Samples for the scientific purpose. This study was financially supported by Research Fellowships for Young Scientists from the Japan Society for the Promotion of Science (JSPS) to K.K. (Grant Number: 17J04576); JSPS Kakenhi grants to K.K. (Grant Number: 18K18186); to T.I. (Grant Number: 16H04066); and to T.S. (Grant Number: 15K21221); Grant for Environmental Research Projects from The Sumitomo Foundation to T.S. (Grant Number: 133303).

Author Contributions

T.Y. obtained the marine sediment core. K.K., Y.Y. and T.S. designed the study and obtained foraminifera samples. K.K. and T.I. measured the Mg/Ca and boron isotope ratios of foraminifera samples. K.K. and M.I. measured oxygen isotope ratios of foraminifera samples. K.K., Y.Y., T.I., T.S., M.I. and T.Y. contributed to the interpretation of the data and the preparation of the final manuscript.

Additional Information

Supplementary information accompanies this paper at <https://doi.org/10.1038/s41598-019-49739-0>.

Competing Interests: The authors declare no competing interests.

Publisher's note Springer Nature remains neutral with regard to jurisdictional claims in published maps and institutional affiliations.



Open Access This article is licensed under a Creative Commons Attribution 4.0 International License, which permits use, sharing, adaptation, distribution and reproduction in any medium or format, as long as you give appropriate credit to the original author(s) and the source, provide a link to the Creative Commons license, and indicate if changes were made. The images or other third party material in this article are included in the article's Creative Commons license, unless indicated otherwise in a credit line to the material. If material is not included in the article's Creative Commons license and your intended use is not permitted by statutory regulation or exceeds the permitted use, you will need to obtain permission directly from the copyright holder. To view a copy of this license, visit <http://creativecommons.org/licenses/by/4.0/>.

© The Author(s) 2019